

THE STAR FORMATION EFFICIENCY PER FREE FALL TIME IN NEARBY GALAXIES

DYAS UTOMO,¹ JIAYI SUN,¹ ADAM K. LEROY,¹ J. M. DIEDERIK KRUIJSSEN,² EVA SCHINNERER,³ ANDREAS SCHRUBA,⁴
FRANK BIGIEL,⁵ GUILLERMO A. BLANC,^{6,7} MÉLANIE CHEVANCE,² ERIC Emsellem,⁸ CINTHYA HERRERA,⁹
ALEXANDER P. S. HYGATE,^{3,2} KATHRYN KRECKEL,³ EVE C. OSTRIKER,¹⁰ JEROME PETY,^{9,11} MIGUEL QUEREJETA,^{8,12}
ERIK ROSOLOWSKY,¹³ KARIN M. SANDSTROM,¹⁴ AND ANTONIO USERO¹²

¹*Department of Astronomy, The Ohio State University, 140 West 18th Ave, Columbus, OH 43210, USA; utomo.6@osu.edu*

²*Astronomisches Rechen-Institut, Zentrum für Astronomie der Universität Heidelberg, Mönchhofstraße 12-14, D-69120 Heidelberg, Germany*

³*Max-Planck-Institut für Astronomie, Königstuhl 17, D-69117 Heidelberg, Germany*

⁴*Max-Planck-Institut für Extraterrestrische Physik, Giessenbachstraße 1, D-85748 Garching bei Muenchen, Germany*

⁵*Institut für Theoretische Astrophysik, Zentrum für Astronomie der Universität Heidelberg, Albert-Ueberle-Straße 2, 69120 Heidelberg, Germany*

⁶*The Observatories of the Carnegie Institution for Science, 813 Santa Barbara Street, Pasadena, CA 91101, USA*

⁷*Departamento de Astronomía, Universidad de Chile, Casilla 36-D, Santiago, Chile*

⁸*European Southern Observatory, Karl-Schwarzschild Straße 2, D-85748 Garching bei München, Germany*

⁹*IRAM, 300 rue de la Piscine, F-38406 Saint Martin d'Hères, France*

¹⁰*Department of Astrophysical Sciences, Princeton University, Peyton Hall, 4th Ivy Lane, Princeton, NJ 08544, USA*

¹¹*Sorbonne Université, Observatoire de Paris, Université PSL, École normale supérieure, CNRS, LERMA, F-75005, Paris, France*

¹²*Observatorio Astronómico Nacional (OAN), C/Alfonso XII 3, Madrid E-28014, Spain*

¹³*Department of Physics, University of Alberta, 4-183 CCIS, Edmonton, AB T6G 2E1, Canada*

¹⁴*Center for Astrophysics and Space Sciences, Department of Physics, University of California, San Diego, 9500 Gilman Drive, La Jolla, CA 92093, USA*

ABSTRACT

We estimate the star formation efficiency per gravitational free fall time, ϵ_{ff} , from observations of nearby galaxies with resolution matched to the typical size of a Giant Molecular Cloud. This quantity, ϵ_{ff} , is theoretically important but so far has only been measured for Milky Way clouds or inferred indirectly in a few other galaxies. Using new, high resolution CO imaging from the PHANGS-ALMA survey, we estimate the gravitational free-fall time at 60 to 120 pc resolution, and contrast this with the local molecular gas depletion time to estimate ϵ_{ff} . Assuming a constant thickness of the molecular gas layer ($H = 100$ pc) across the whole sample, the median value of ϵ_{ff} in our sample is 0.7%. We find a mild scale-dependence, with higher ϵ_{ff} measured at coarser resolution. Individual galaxies show different values of ϵ_{ff} , with the median ϵ_{ff} ranging from 0.3% to 2.6%. We find the highest ϵ_{ff} in our lowest mass targets, reflecting both long free-fall times and short depletion times, though we caution that both measurements are subject to biases in low mass galaxies. We estimate the key systematic uncertainties, and show the dominant uncertainty to be the estimated line-of-sight depth through the molecular gas layer and the choice of star formation tracers.

Keywords: galaxies: ISM — galaxies: spiral — galaxies: star formation — ISM: molecules

1. INTRODUCTION

Star formation is “inefficient,” meaning that the star formation rate is low compared to what would be expected if cold gas collapsed directly into stars (see review by McKee & Ostriker 2007; Krumholz 2014). Theoretical models of star formation in molecular clouds that attempt to explain this inefficiency include turbulent support (Krumholz & McKee 2005; Padoan et al. 2012), destructive feedback (Murray et al. 2010), magnetic fields (Federrath 2015), and dynamical stabilization (Ostriker et al. 2010; Meidt et al. 2018).

Over the last decade, many of these models have expressed their predictions in terms of the *efficiency of star formation per free fall time*, ϵ_{ff} . This ϵ_{ff} is the fraction of gas converted

into stars per gravitational free fall time, τ_{ff} . As such, ϵ_{ff} expresses the inefficiency of star formation relative to free-fall collapse. Theoretical predictions for ϵ_{ff} on cloud scales span the range from $\sim 0.1\%$ to few times 10% (McKee & Ostriker 2007; Krumholz et al. 2012; Federrath & Klessen 2012; Padoan et al. 2012; Raskutti et al. 2016), with higher values possible for clouds with active star formation (Murray 2011; Lee et al. 2016) or the densest parts of clouds (Evans et al. 2014). From numerical simulations, ϵ_{ff} increases strongly from low values in unbound gas to high values when the virial parameter is near unity (Padoan et al. 2012).

In spite of the fact that ϵ_{ff} is the central prediction of many current models of star formation, observational constraints

on this quantity have remained challenging. The issue is that τ_{ff} depends on the volume density of the gas, ρ , via

$$\tau_{\text{ff}} = \sqrt{\frac{3\pi}{32G\rho}}, \quad (1)$$

and it is difficult to directly measure ρ at cloud scales. This requires either high resolution imaging or density-sensitive multi-line spectroscopy (Gao & Solomon 2004a; Leroy et al. 2017b).

Indirect estimates of ϵ_{ff} are common. For example, Murray (2011), Evans et al. (2014), Lee et al. (2016), and Vutisalchavakul et al. (2016) estimated $\epsilon_{\text{ff}} \approx 0.4\text{--}1.6\%$ for populations of star-forming clouds in the Milky Way (MW), and Barnes et al. (2017) obtained $\epsilon_{\text{ff}} \approx 1\text{--}4\%$ in the central few hundred parsec of the MW. Ochsendorf et al. (2017) extended such studies to the Large Magellanic Cloud, where they found ϵ_{ff} in the range of 12–25% (depending on the adopted SFR tracer) and showed that ϵ_{ff} decreases with increasing cloud mass. The above findings for ϵ_{ff} are mean values; all of the above studies of individual GMCs (as well as earlier work by Mooney & Solomon 1988) showed a large range of efficiency, much of which maybe due to cloud’s evolution. Leroy et al. (2017a) estimated $\epsilon_{\text{ff}} \approx 0.30\text{--}0.36\%$ in M51, based on the PAWS survey (Schinnerer et al. 2013), and Schrubba et al. (2018b) found $\epsilon_{\text{ff}} \approx 0.1\text{--}1\%$ in the MW and 7 nearby galaxies. However, we still lack a statistically significant sample of ϵ_{ff} across the local galaxy population.

The most general measurement to date comes from observations of dense gas, as traced by high critical density line emission (e.g., HCN; Gao & Solomon 2004b). By equating the mean gas density of an emission line with its critical density, and adopting a dense gas conversion factor, they can infer ϵ_{ff} . This approach has been taken by Krumholz & Tan (2007) and García-Burillo et al. (2012), who concluded that ϵ_{ff} is approximately constant (0.5–1%). Subsequently, numerous other studies (Longmore et al. 2013; Kruijssen et al. 2014; Usero et al. 2015; Bigiel et al. 2016; Gallagher et al. 2018) have used similar techniques to find an environmentally-dependent ϵ_{ff} (0.2–4%).

The PHANGS¹ collaboration is now using ALMA to map the molecular gas in 74 nearby galaxies with resolution matched to the scale of an individual Giant Molecular Cloud. These observations recover the surface density of molecular gas at high physical resolution, which is closely related to the mean volume density. In this Letter, we combine the first 11 CO(2–1) maps from PHANGS-ALMA with three CO maps from the literature. From these maps, we infer τ_{ff} and compare it to the measured gas depletion time to estimate ϵ_{ff} . This yields the largest and most direct sample of extragalactic ϵ_{ff}

measurements to date. After describing our data in §2 and explaining our methodology in §3, we present the key results in §4 and summarize them in §5.

2. DATA

2.1. Molecular Gas

We estimate molecular gas surface density from PHANGS-ALMA CO (2–1) data for 11 targets and archival CO data for M31 (A. Schrubba et al. in preparation; Caldú-Primo & Schrubba 2016), M33 (Druard et al. 2014), and M51 (Schinnerer et al. 2013). PHANGS-ALMA uses ALMA’s 12m, 7m, and total power antennas to map CO (2–1) emission from nearby ($d \lesssim 17$ Mpc) galaxies at native angular resolution of 1–1.5". This translates to native physical resolutions of $\sim 60\text{--}120$ pc depending on the distance to the target. At their native resolutions, the CO data cubes have rms noise of ~ 0.1 K per 2.5 km s^{−1} channel. The inclusion of the ACA 7m and total power data means that we expect these maps to be sensitive to emission at all spatial scales.

The sample selection, observing strategy, reduction, and properties of the full 74 galaxies in PHANGS-ALMA survey is presented in A. K. Leroy et al. (in preparation). Here, we use the first data sets, including three literature maps, where the CO surface brightness and line-width have been calculated by Sun et al. (2018). See that paper for a detailed presentation of masking, map construction, and completeness.

We adopt a fixed CO(2–1)-to-H₂ conversion factor $\alpha_{\text{CO}}^{2-1} = 6.2 M_{\odot} \text{pc}^{-2} (\text{K km s}^{-1})^{-1}$. This combines the commonly adopted Galactic CO(1–0) conversion factor, $\alpha_{\text{CO}}^{1-0} = 4.35 M_{\odot} \text{pc}^{-2} (\text{K km s}^{-1})^{-1}$ (Bolatto et al. 2013), including the contribution from Helium, with a typical CO(2–1)/CO(1–0) line ratio of 0.7 (e.g., Sakamoto et al. 1997; Leroy et al. 2013). Then, we convert the CO(2–1) integrated intensity, I_{CO}^{2-1} , to Σ_{mol} via:

$$\Sigma_{\text{mol}} [M_{\odot} \text{pc}^{-2}] = \alpha_{\text{CO}}^{2-1} I_{\text{CO}}^{2-1} [\text{K km s}^{-1}], \quad (2)$$

The M31 and M51 CO maps target the CO(1–0) line. For those we use $\alpha_{\text{CO}}^{1-0} = 4.35 M_{\odot} \text{pc}^{-2} (\text{K km s}^{-1})^{-1}$ with no line ratio term. We apply inclination corrections to all measured surface densities.

Our sample includes a few low mass (down to $4 \times 10^9 M_{\odot}$), low metallicity galaxies. We explore the effect of a metallicity-dependent α_{CO} on our results for these cases. The fraction of ‘CO-dark’ molecular gas increases with decreasing metallicity, resulting in higher α_{CO} (Bolatto et al. 2013). We use metallicities compiled by Pilyugin et al. (2004, their Table 5), except for M33 and M51, where we adopt metallicities from Rosolowsky & Simon (2008) and Croxall et al. (2015), respectively, and NGC 1672, NGC 3627, and NGC 4535, for which we adopt metallicities from K. Kreckel et al. in preparation based on new VLT-MUSE observations. All metallicities are quoted at 0.4 R_{25} . We calculate the

¹ <http://www.phangs.org>

metallicity-dependent α_{CO} following the prescription of [Bolatto et al. \(2013\)](#). Beyond metallicity effects, the central regions of many galaxies shows smaller α_{CO} ([Sandstrom et al. 2013](#)). Our key result in this paper is weighted by area and the center covers only a few lines-of-sight, so we defer investigation of the impact of this effect to future papers.

2.2. Recent Star Formation

We derive the star formation rate (SFR) surface density, Σ_{SFR} , from WISE infrared and GALEX UV maps (A. K. Leroy et al. in preparation). The WISE maps are derived from the unWISE reprocessing of [Lang \(2014\)](#). The GALEX maps are coadded, convolved, background subtracted maps constructed from the full-mission GALEX archive ([Martin & GALEX Team 2005](#)). We correct the FUV and NUV maps for Galactic extinction using $E(B-V)$ from the map of [Schlegel et al. \(1998\)](#) converted to the GALEX bands using the R_{NUV} and R_{FUV} values from [Peek & Schiminovich \(2013\)](#). Both sets of maps are convolved to have matched Gaussian beams ($15''$ FWHM, which corresponds to 1.3 kpc at our most distant target) and background-subtracted using control regions outside the galaxy.

We convert FUV, NUV, $12\mu\text{m}$, and $22\mu\text{m}$ intensity, I_ν , to an estimate of the recent SFR using

$$\Sigma_{\text{SFR}} [\text{M}_\odot \text{ yr}^{-1} \text{ kpc}^{-2}] \approx K I_\nu [\text{MJy sr}^{-1}], \quad (3)$$

where $K = 1.04 \times 10^{-1}$, 1.04×10^{-1} , 3.77×10^{-3} , and 2.97×10^{-3} for FUV, NUV, $12\mu\text{m}$, and $24\mu\text{m}$ bands, respectively ([Kennicutt & Evans 2012](#); [Jarrett et al. 2013](#)). We use hybrid tracers by adding the SFR derived from each choice of UV and IR band, and adopt $\text{SFR}(\text{FUV}+22\mu\text{m})$ as a benchmark. To estimate systematic uncertainties, we test the effect of using NUV instead of FUV and using $12\mu\text{m}$ instead of $22\mu\text{m}$.

3. METHODOLOGY

We estimate ϵ_{ff} from the ratio between the gravitational free fall time of molecular gas, τ_{ff} , and the molecular gas depletion time, $\tau_{\text{dep}}^{\text{mol}}$.

3.1. Molecular Gas Depletion Time

We calculate $\tau_{\text{dep}}^{\text{mol}}$ at 1.3 kpc resolution across each target as

$$\tau_{\text{dep}, 1.3\text{kpc}}^{\text{mol}} = \frac{\Sigma_{\text{mol}, 1.3\text{kpc}}}{\Sigma_{\text{SFR}, 1.3\text{kpc}}}. \quad (4)$$

Here, $\Sigma_{\text{mol}, 1.3\text{kpc}}$ is the convolved Σ_{mol} at 1.3 kpc FWHM to match the resolution of $\Sigma_{\text{SFR}, 1.3\text{kpc}}$ maps. We treat this as our working resolution to estimate $\tau_{\text{dep}}^{\text{mol}}$.

3.2. Molecular Gas Free Fall Time

We estimate τ_{ff} following Equation 1. This requires an estimate of the mass volume density, ρ . To estimate ρ , we combine our measured, high physical resolutions (60–120 pc)

Σ_{mol} with an estimate of the line-of-sight depth through the molecular gas layer, H , so that:

$$\rho \approx \frac{\Sigma_{\text{mol}}}{H}. \quad (5)$$

We describe how we estimate H in §3.3. We combine Equations 1 and 5 to estimate τ_{ff} as

$$\tau_{\text{ff}, 60\text{pc}} = \sqrt{\frac{3\pi}{32G} \left(\frac{H}{\Sigma_{\text{mol}, 60\text{pc}}} \right)}. \quad (6)$$

We make analogous measurements of τ_{ff} at 80, 100, and 120 pc resolution, as permitted by the native resolution of the data.

3.3. Thickness of the Molecular Gas Layer

To translate a measured molecular gas surface density into a volume density, we must estimate the line of sight depth of the molecular gas layer, H . We define H so that $\rho = \Sigma_{\text{mol}}/H$. We explore three approaches:

1. *Fixed $H = 100$ pc.* This is roughly the diameter of a large molecular cloud and a characteristic thickness (FWHM) of the molecular gas layer in the Milky Way and other galaxies ([Heyer & Dame 2015](#); [Yim et al. 2014](#); [Pety et al. 2013](#)). This is our default value.
2. In *hydrostatic equilibrium*, the turbulent midplane pressure of molecular gas balances the vertical weight of the molecular gas column in the potential of the disk. If we consider only gas responding to the potential well defined by stars, i.e., neglecting gas self-gravity, then

$$H \equiv 2h \approx \sqrt{\frac{\sigma_{\text{mol}}^2 h_*}{G \Sigma_*}}, \quad (7)$$

following [Ostriker et al. \(2010\)](#). Here σ_{mol} is the velocity dispersion of the molecular gas, Σ_* is the mass surface density of stars, and h_* is the stellar scale height ($\rho_* = \Sigma_*/2h_*$). Here, we adopt a typical $h_* = 300$ pc, use the measured line width from [Sun et al. \(2018\)](#), and estimate Σ_* from the dust-corrected *Spitzer* $3.6\mu\text{m}$ maps produced by [Querejeta et al. \(2015\)](#)² assuming a mass-to-light ratio of $0.5 M_\odot/L_\odot$ ([Meidt et al. 2014](#)). The median of H under this assumption is 122 pc.

3. We assume that each beam contains one spherical, *unresolved cloud in energy equipartition*. In this

² In four galaxies, we currently lack *Spitzer* maps and use WISE $3.4\mu\text{m}$ maps instead.

case, kinetic energy balances gravitational potential energy, equivalent to setting the virial parameter $\alpha_{\text{vir}} \approx 2$ (Bertoldi & McKee 1992; Sun et al. 2018). We take $\alpha_{\text{vir}} \approx (5\sigma_{\text{mol}}^2 R)/(GM_{\text{mol}})$ and calculate the mass in the beam from $M_{\text{mol}} = \Sigma_{\text{mol}} A$, where $A = \pi(\theta_{\text{FWHM}}/2)^2/\ln 2$ is the physical beam area. From this, we derive the cloud diameter, $2R$, via

$$H \equiv 2R \approx \frac{2\alpha_{\text{vir}} G \Sigma_{\text{mol}} A}{5\sigma_{\text{mol}}^2}. \quad (8)$$

The median of H under this assumption is 116 pc.

We calculate H using each method above and compare the resulting ϵ_{ff} to estimate the systematic uncertainty associated with estimating H .

3.4. Combining Scales

We estimate τ_{ff} at 60–120 pc resolution and measure $\tau_{\text{dep}}^{\text{mol}}$ at 1.3 kpc resolution. To combine these measurements, we calculate the mass-weighted average of τ_{ff} within each 1.3 kpc region of a galaxy. This is equivalent to asking ‘‘What is the mass-weighted mean of τ_{ff} of a parcel of molecular gas in this kpc-sized region of this galaxy?’’ Figure 1 illustrates our approach for one of our targets, NGC 628.

We calculate the mass-weighted mean of τ_{ff}^{-1} via

$$\langle \tau_{\text{ff},60\text{pc}}^{-1} \rangle_{1.3\text{kpc}} = \frac{\tau_{\text{ff},60\text{pc}}^{-1} \Sigma_{\text{mol},60\text{pc}} * \theta_{60\text{pc}}^{1.3\text{kpc}}}{\Sigma_{\text{mol},60\text{pc}} * \theta_{60\text{pc}}^{1.3\text{kpc}}}, \quad (9)$$

where $\Sigma_{\text{mol},60\text{pc}}$ is the surface density of molecular gas at 60 pc resolution, $\theta_{60\text{pc}}^{1.3\text{kpc}}$ is the Gaussian kernel to convolve a 60 pc resolution map to 1.3 kpc resolution, and $*$ denotes convolution. We have round Gaussian beams in all maps.

Hereby, we assume that $\langle \tau_{\text{ff},60\text{pc}}^{-1} \rangle_{1.3\text{kpc}} \approx \langle \tau_{\text{ff},60\text{pc}}^{-1} \rangle_{1.3\text{kpc}}$.

This differs slightly from Leroy et al. (2017a). They first calculated the mass-weighted mean of *surface density*, and then used that to calculate τ_{ff} , instead of directly calculating the mass-weighted mean of τ_{ff}^{-1} . The approach here should yield a more rigorous comparison to predictions in which $\Sigma_{\text{SFR}} = \epsilon_{\text{ff}} \Sigma_{\text{mol}}/\tau_{\text{ff}}$. The two approaches yield qualitatively similar results, though, with the mean $\langle \tau_{\text{ff},60\text{pc}} \rangle_{1.3\text{kpc}}$ differing by only $\sim 7\%$.

3.5. Star Formation Efficiency per Free Fall Time

We calculate ϵ_{ff} as the ratio between τ_{ff} and $\tau_{\text{dep}}^{\text{mol}}$,

$$\langle \epsilon_{\text{ff},60\text{pc}} \rangle_{1.3\text{kpc}} = \frac{\langle \tau_{\text{ff},60\text{pc}} \rangle_{1.3\text{kpc}}}{\tau_{\text{dep},1.3\text{kpc}}^{\text{mol}}}. \quad (10)$$

We carry out analogous calculations at 80, 100, and 120 pc resolutions. This allows us to study the impact of varying the linear resolution on the measured values of ϵ_{ff} . Our targets vary in their native physical resolutions, so not all targets are available at the highest resolutions (Sun et al. 2018).

3.6. Correction for Incompleteness

When estimating $\langle \tau_{\text{ff},60\text{pc}} \rangle_{1.3\text{kpc}}$, we begin with a high resolution map that has been masked using a signal-to-noise cut (Sun et al. 2018). The calculation will miss emission at signal-to-noise below this cut, which has preferentially low Σ_{mol} and long τ_{ff} . Sun et al. (2018) measured the degree of this effect for each of our maps. They define the completeness, C , as the fraction of the total CO flux, measured at lower resolution with very good signal-to-noise, that is included in the high resolution, masked map. For our targets, C ranges from 44% to 96% at 120 pc resolution, and is typically lower at finer resolutions.

To estimate the effect of incompleteness on our calculated τ_{ff} , we use a Monte Carlo approach. We randomly draw 10^6 samples from a lognormal distribution designed to simulate the true distribution of mass as a function of Σ_{mol} (see Leroy et al. 2016; Sun et al. 2018). These model distributions have 1σ width of 0.5 dex. For each distribution, we calculate true expectation value of τ_{ff}^{-1} weighted by Σ_{mol} , for the whole distribution and for subsets of the sample where only the highest fraction C of the data are included.

This yields a correction factor f_C , defined as the ratio of the true $\langle \tau_{\text{ff}} \rangle$ over the measured $\langle \tau_{\text{ff}} \rangle$, as a function of C . We apply these to the data based on the value of C measured in each 1.3 kpc larger beam (our flux recovery is nearly perfect at 1.3 kpc resolution; Leroy et al. 2016; Sun et al. 2018). Incompleteness suppresses faint, long τ_{ff} lines-of-sight, so that $1.0 \lesssim f_C \lesssim 1.1$ for 120 pc beam. Therefore, correcting for incompleteness increases τ_{ff} and ϵ_{ff} .

4. RESULTS

In the left panel of Figure 2 and Table 1, we summarize our measurements of ϵ_{ff} for the whole sample, using our standard assumption ($H = 100$ pc, SFR from FUV+22 μm , incomplete, and Galactic α_{CO}). These measurements over a large area across 14 galaxies represent the most complete measurement of the efficiency of star formation per free fall time to date. At 120 pc resolution (red histogram), we find median $\epsilon_{\text{ff}} \approx 0.7\%$ across all lines-of-sight in 14 galaxies, with the 16–84% percentile range spanning $\epsilon_{\text{ff}} \approx 0.4\text{--}1.1\%$.

The number of lines-of-sight varies in each galaxy. If instead, we take a median value for each galaxy, and compute the overall median across the whole sample (equivalent to giving equal weight to each galaxy), then $\epsilon_{\text{ff}} \approx 0.8\%$. Those ϵ_{ff} values are the most fundamental result of this letter.

4.1. Uncertainties

The histograms in Figure 2 combine more than 940 regions of 1.3 kpc in size (see Table 1), and the statistical uncertainties on any given ϵ_{ff} estimate tend to be quite small ($\lesssim 0.01$ dex), because many measurements are already averaged together within each 1.3 kpc beam. As a result, we

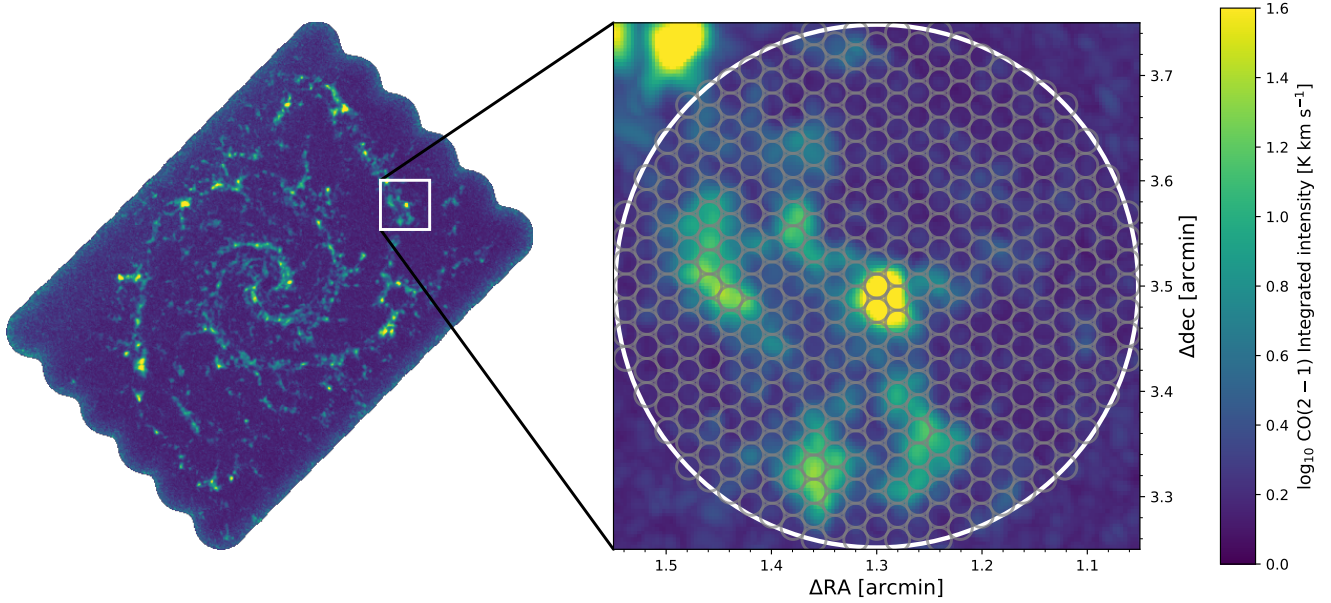


Figure 1. *Left:* CO(2–1) integrated intensity map of NGC 628 at 60 pc resolution (color codes in the range of $0.0 \leq \log_{10}[\text{CO}(2-1)/\text{K km s}^{-1}] \leq 1.6$). We use this map to estimate molecular gas surface density and free-fall time. *Right:* Illustration of our cross-scale methodology. We measure the molecular gas depletion time, $\tau_{\text{dep}} \equiv \Sigma_{\text{mol}}/\Sigma_{\text{SFR}}$ at 1.3 kpc resolution (illustrated by the large circle). Within each 1.3 kpc region, we calculate Σ_{mol} and τ_{ff} for each 60 pc beam (small circles). We average these high resolution τ_{ff} estimates within 1.3 kpc region, weighted by Σ_{mol} at 60 pc beam. By dividing τ_{ff} by $\tau_{\text{dep}}^{\text{mol}}$, we calculate the average ϵ_{ff} within each 1.3 kpc region while still leveraging the high resolution of the PHANGS-ALMA CO maps.

Table 1. Measurements summary for all lines-of-sight.

Quantities	Physical resolutions of CO maps			
	60 pc	80 pc	100 pc	120 pc
Numbers of galaxies	9	9	11	14
Numbers of lines-of-sight	949	949	1651	2937
Median of $\langle \epsilon_{\text{ff}} \rangle$	0.63%	0.72%	0.70%	0.71%
16 th percentile of $\langle \epsilon_{\text{ff}} \rangle$	0.40%	0.44%	0.38%	0.39%
84 th percentile of $\langle \epsilon_{\text{ff}} \rangle$	1.00%	1.15%	1.15%	1.15%
Median of $\langle \tau_{\text{ff}} \rangle$ [Myr]	11.16	12.68	12.54	11.79
16 th percentile of $\langle \tau_{\text{ff}} \rangle$ [Myr]	6.52	7.04	7.29	7.57
84 th percentile of $\langle \tau_{\text{ff}} \rangle$ [Myr]	13.62	15.74	15.75	15.59
Median of τ_{dep} [Gyr]	1.72	1.72	1.77	1.69
16 th percentile of τ_{dep} [Gyr]	1.18	1.18	1.13	1.11
84 th percentile of τ_{dep} [Gyr]	2.29	2.29	2.41	2.35

expect that the spread in the histogram to represent real physical variations in ϵ_{ff} from region to region and from galaxy to galaxy. The dominant uncertainties affecting the measurement are systematic. We explore the magnitude of these systematic uncertainties in the right panel of Figure 2, where we vary our adopted SFR tracer, the line-of-sight depth, completeness correction, the CO-to-H₂ conversion factor, and linear resolution.

In general, over the range of assumptions that we explore, systematic effects can shift ϵ_{ff} by ~ 0.1 dex. In particular, altering our mix of SFR tracers shifts ϵ_{ff} by $\lesssim 0.1$ dex. Adopt-

ing a metallicity-dependent α_{CO} only has a small impact on the median ϵ_{ff} of the whole sample because our low mass galaxies contribute only a small fraction of the total lines-of-sight. However, variations in α_{CO} have a more significant impact on the measured ϵ_{ff} in individual galaxies (§4.3).

Varying the resolution of the maps changes ϵ_{ff} , but only weakly. Within our sample, changing the resolution from 60 to 120 pc increases ϵ_{ff} by ~ 0.1 dex. This is consistent with the idea that beam dilution decreases the measured Σ_{mol} as the resolution degrades, which in turn raises τ_{ff} and ϵ_{ff} . Other systematic uncertainties stem from imperfect knowledge of the disk thickness, H , and incompleteness due to limited sensitivity in the high resolution CO maps. The right panel of Figure 2 shows that correcting for the presence of low Σ_{mol} , high τ_{ff} lines-of-sight shifts ϵ_{ff} towards higher value by < 0.1 dex. Meanwhile, adopting different plausible treatments of H can also shift ϵ_{ff} by $\lesssim 0.1$ dex. Direct measurements of the vertical distribution of the cold gas in galaxies (Yim et al. 2011, 2014) will help to constraint H and ϵ_{ff} .

4.2. Comparison to Previous Studies

We find $\epsilon_{\text{ff}} \approx 0.7\% \pm 0.3\%$. This value is comparable to the often-quoted theoretical values of $\approx 1\%$ (McKee & Ostriker 2007; Krumholz & Tan 2007; Krumholz et al. 2012). Numerical simulations of kpc-scale regions of the ISM with star formation feedback found $\epsilon_{\text{ff}} \approx 0.6\%$ (Kim et al. 2013); this can be understood based on expectations from UV heating and

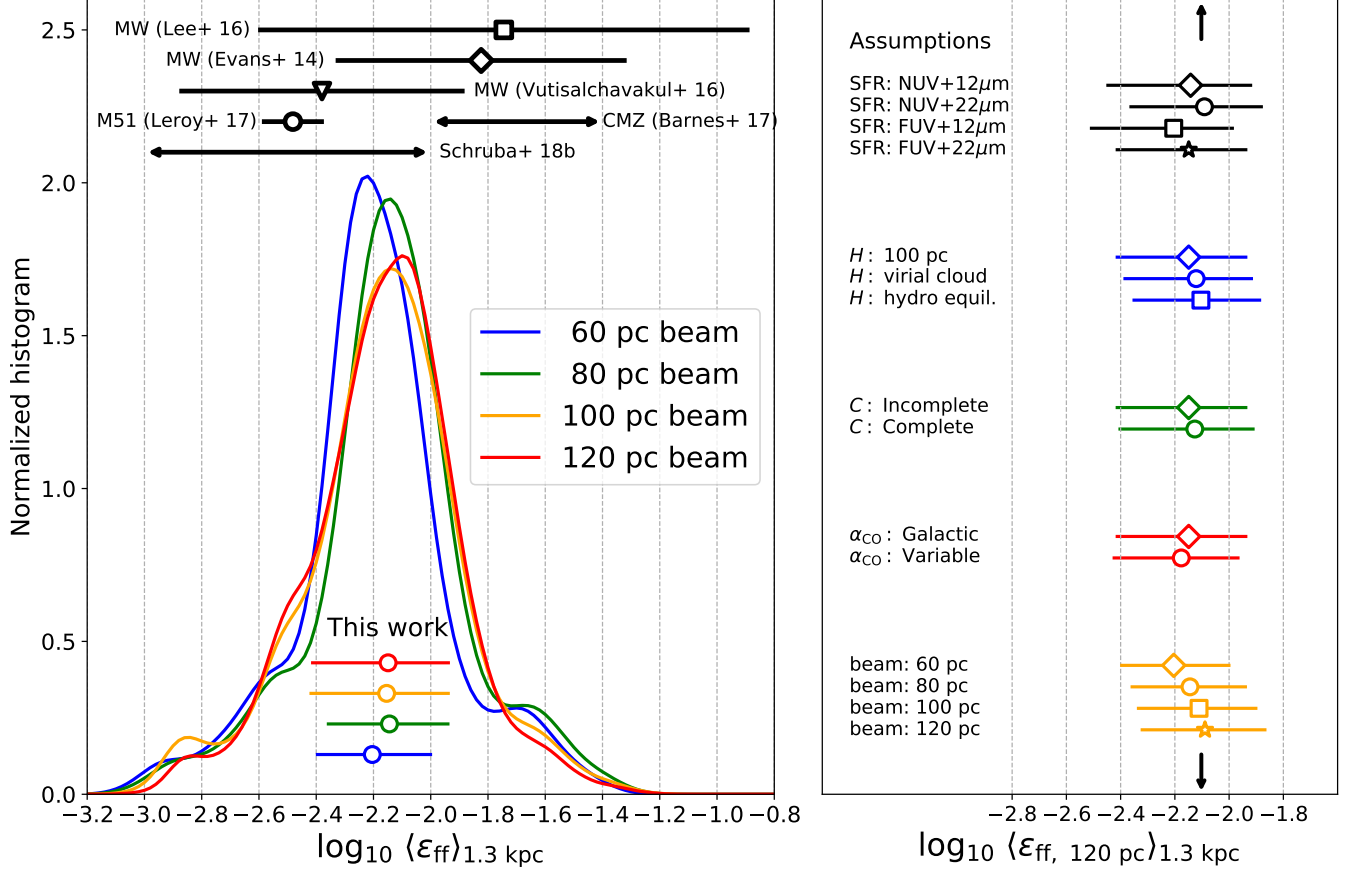


Figure 2. Efficiency per free fall time in 14 galaxies. *Left:* histograms of ϵ_{ff} for all regions studied (smoothed using a Gaussian kernel density estimator following Scott 1992). The histograms combine all galaxies and give equal weight to each 1.3 kpc region regardless of galaxy or other properties. Different colors show results for τ_{ff} calculated at different resolutions. Circles and lines mark the median, 16th, and 84th percentile ϵ_{ff} for each resolution. For comparison, we show the values of ϵ_{ff} measured for Milky Way clouds (Evans et al. 2014; Lee et al. 2016), in the Central Molecular Zone (Barnes et al. 2017), in M51 at 40 pc resolution (Leroy et al. 2017a), and a compilation study for MW and 7 nearby galaxies (Schruha et al. 2018b). *Right:* Impact of assumptions and uncertainties. We plot the median and 16th–84th percentile range of $\langle \epsilon_{\text{ff}} \rangle$ by altering various assumptions from our default values at 120 pc resolution. For various linear resolutions, we only include 9 galaxies that can be resolved down to 60 pc. Most systematic uncertainties affect the results at the ~ 0.1 dex ($\sim 25\%$) level. The choices of SFR tracers and beam sizes have the largest impact. We also plot the median $\langle \epsilon_{\text{ff}} \rangle$, giving equal weight for each galaxy, as small vertical arrows.

turbulence driving by supernovae (Ostriker et al. 2010; Ostriker & Shetty 2011). Our ϵ_{ff} value is lower than $\epsilon_{\text{ff}} \approx 10\%$ suggested by Agertz & Kravtsov (2015), but they also argued that their high *local* efficiency is derived from a short cloud-scale $\tau_{\text{dep}}^{\text{mol}}$ (rather than kpc-scales as in our work), and can still result in a low apparent *global* efficiency ($\sim 0.25\%$) if a global (kpc-scales) $\tau_{\text{dep}}^{\text{mol}}$ of ~ 2 Gyrs (Leroy et al. 2013; Utomo et al. 2017, this work) is adopted.

As Figure 2 shows, our measured ϵ_{ff} is low compared to the median $\epsilon_{\text{ff}} \sim 1.5\text{--}1.8\%$ found in the Milky Way (MW) clouds by Evans et al. (2014), Lee et al. (2016), and Barnes et al. (2017). This can be partially understood because the focus of MW measurements is on the high column density parts of clouds (Evans et al. 2014) and on actively star forming clouds (Lee et al. 2016). Evans et al. measured ϵ_{ff} within a visual extinction contour of $A_V > 2$ magnitude (equivalent

to $\Sigma_{\text{mol}} \gtrsim 20 M_{\odot} \text{ pc}^{-2}$). Our measurements also integrate over lower column density regions, resulting in τ_{ff} and $\tau_{\text{dep}}^{\text{mol}} \sim 8$ and 16 times longer than those in Evans et al. Indeed, Vutisalchavakul et al. (2016) found a mean $\epsilon_{\text{ff}} \approx 0.4\%$ by considering a sample of lower volume density of MW clouds (with mean $n_{\text{H}_2} \sim 300 \text{ cm}^{-3}$, instead of 800 cm^{-3} as in Evans et al.).

Furthermore, we expect the difference with the Lee et al. (2016) MW measurements to reflect a bias towards actively star forming clouds in their sample (e.g., Kruijssen & Longmore 2014; Kruijssen et al. 2018, §2.1). Their measurements include $\sim 80\%$ of the ionizing photon flux in the MW, but only captured $\sim 10\%$ of the total GMC mass in the Miville-Deschênes et al. (2017) catalog. Our measurements include all CO emission in each 1.3 kpc aperture, so that clouds and star forming regions in all evolutionary states are included (as

long as they are above the sensitivity limit). Following Murray (2011), Lee et al. (2016) emphasized the large scatter of ϵ_{ff} from cloud to cloud (a result that goes back to Mooney & Solomon 1988). Our 1.3 kpc $\tau_{\text{dep}}^{\text{mol}}$ measurements average over many clouds and so neither contradict nor confirm their result. Cloud-by-cloud star formation rate estimates are in progress for PHANGS (e.g., K. Kreckel et al. in preparation), and will help to test whether the observations of Murray (2011) and Lee et al. (2016) indeed hold in other galaxies.

Our median $\epsilon_{\text{ff}} \approx 0.7\%$ in the whole sample is about twice the $\epsilon_{\text{ff}} \approx 0.30\text{--}0.36\%$ found by Leroy et al. (2017a) using an almost identical methodology to study M51 at 40 pc resolution. M51 is also part of our sample, and our measurements for that galaxy agree well with those in Leroy et al. (2017a). This appears to reflect a real difference between M51 and the rest of our sample, i.e. M51 has the lowest ϵ_{ff} of any galaxy in our sample. Following Meidt et al. (2013), this may reflect strong gas flows in M51 that act to stabilize the gas and suppress star formation. Strong gas flows were also observed in NGC 3627 (Beuther et al. 2017), where ϵ_{ff} is low ($\approx 0.6\%$).

4.3. Galaxy-to-Galaxy Variations

Figure 2 shows overall results for the whole sample, but we also observe strong galaxy-to-galaxy variations in ϵ_{ff} . In Figure 3 and Table 2, we report ϵ_{ff} for each galaxy at 120 pc resolution. Red circles and bars show the median and 16th–84th percentile range for each galaxy using a Galactic α_{CO} . Here, the contrast between low mass, low metallicity galaxies and massive galaxies stands out. To illuminate a possible cause for this, we also show results adopting metallicity-dependent α_{CO} as gray circles. Because ϵ_{ff} depends on both $\tau_{\text{dep}}^{\text{mol}}$ and τ_{ff} , we also plot these quantities in the middle and lower panels.

The top panel of Figure 3 shows a dynamic range of an order of magnitude in ϵ_{ff} ($\approx 0.3\text{--}2.6\%$) across our sample. Among the high mass galaxies (excluding M31 and M51), the scatter in ϵ_{ff} is ~ 0.2 dex. Except for M31, ϵ_{ff} appears to decrease with increasing stellar mass of the galaxy (Spearman rank correlation coefficient, $r_s \approx -0.75$).

The middle and bottom panels show that this trend originates from a combination of changes in $\tau_{\text{dep}}^{\text{mol}}$ and τ_{ff} . For Galactic α_{CO} , our three lowest mass galaxies show the shortest $\tau_{\text{dep}}^{\text{mol}}$ in our sample ($\lesssim 1$ Gyr). A similar $\tau_{\text{dep}}^{\text{mol}}\text{--}M_{\star}$ trend was also observed by Saintonge et al. (2011), Leroy et al. (2013), and Bolatto et al. (2017). Meanwhile, τ_{ff} declines with increasing stellar mass ($r_s \approx -0.64$; excluding M31). This agrees with the observation that at a fixed resolution, Σ_{mol} scales with galaxy stellar mass (Sun et al. 2018), leading to longer τ_{ff} in low mass galaxies.

Much, but not all, of the observed trends with stellar mass can be explained by the application of a metallicity dependent α_{CO} , shown as the gray points. If a large reservoir of CO-dark molecular gas is present in these low mass galax-

ies (e.g., Leroy et al. 2011; Bolatto et al. 2013; Gratier et al. 2017; Schruba et al. 2017), then $\tau_{\text{dep}}^{\text{mol}}$ will be longer and τ_{ff} shorter, resulting in lower ϵ_{ff} in the low mass galaxies. The correction that we adopt, which is uncertain, yields $\epsilon_{\text{ff}} \sim 1\%$ in the low mass targets, similar to ϵ_{ff} in the high mass galaxies. However, even with this metallicity correction, there is still a significant anti-correlation between galaxy stellar mass and ϵ_{ff} ($r_s \approx -0.57$; excluding M31).

M31 shows a higher ϵ_{ff} that can not be explained by the metallicity-dependent α_{CO} only. This apparent high efficiency may partially reflect beam-filling effects. M31 has a low molecular-to-atomic gas fraction, and if the clouds are small, widely spaced, and tenuous compared to the beam (as suggested by Sun et al. 2018), then the long τ_{ff} may be partially an observational bias due to low beam filling factor.

5. SUMMARY

We estimate the star formation efficiency per gravitational free-fall time, ϵ_{ff} , in 14 star-forming galaxies, where 11 of them are part of the PHANGS-ALMA survey. This represents the most complete measurement of this key theoretical quantity across local galaxies to date. To do so, we use high resolution CO maps to infer the molecular gas volume density and free-fall time, τ_{ff} , at 60–120 pc resolution. We estimate the gas depletion time from the same CO maps and archival UV and IR data, convolved to 1.3 kpc resolution. We connect those cross-scale measurements by taking the mass-weighted average of τ_{ff}^{-1} within 1.3 kpc aperture.

Overall, we find ϵ_{ff} in the range of 0.4–1.1%, with median $\approx 0.7\%$, and significant galaxy-to-galaxy scatter (0.3–2.6%). We assess the impact of systematic uncertainties on this measurement to be within 0.1 dex, with the largest uncertainties associated with the assumption of molecular gas thickness and the choice of SFR tracer. The galaxy-to-galaxy scatter in ϵ_{ff} is systematic, with an overall trend toward finding higher ϵ_{ff} in low mass galaxies and in our only “green valley” target, M31. We argue that these trends may be partially explained by a metallicity-dependent α_{CO} and sparse, small clouds in M31.

This Letter makes use of the following ALMA data: ADS/JAO.ALMA #2013.1.00925.S #2011.1.00650.S, and #2013.1.00956.S. ALMA is a partnership of ESO (representing its member states), NSF (USA) and NINS (Japan), together with NRC (Canada), NSC and ASIAA (Taiwan), and KASI (Republic of Korea), in cooperation with the Republic of Chile. The Joint ALMA Observatory is operated by ESO, AUI/NRAO, and NAOJ. The National Radio Astronomy Observatory is a facility of the National Science Foundation operated under cooperative agreement by Associated Universities, Inc.

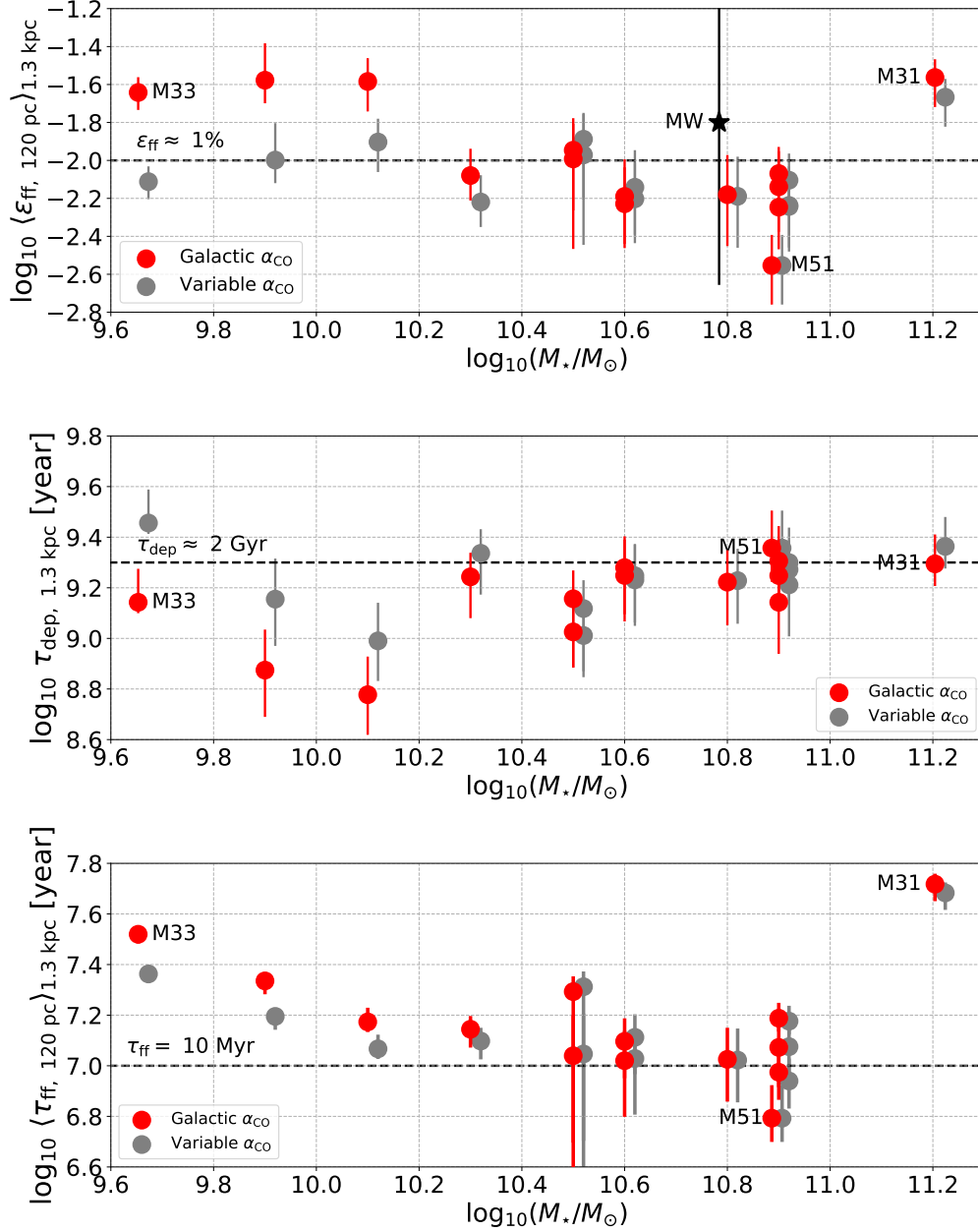


Figure 3. Galaxy-by-galaxy measurements of ϵ_{ff} , $\tau_{\text{dep}}^{\text{mol}}$, and τ_{ff} . *Top panel:* Median and 16th–84th percentile range of ϵ_{ff} for each galaxy as a function of galaxy stellar mass (M_*) for Galactic α_{CO} (red circles and bars) and a metallicity-dependent α_{CO} (gray circles and bars). We shift the gray circles to the right by 0.02 dex for clarity. *Middle and bottom panels:* same as the top panel, but for $\tau_{\text{dep}}^{\text{mol}}$ and τ_{ff} .

The work of DU, AKL, and JS is partially supported by the National Science Foundation under Grants No. 1615105, 1615109, and 1653300. JMDK and MC gratefully acknowledge funding from the German Research Foundation (DFG) in the form of an Emmy Noether Research Group (grant number KR4801/1-1). JMDK gratefully acknowledges funding from the European Research Council (ERC) under the European Union’s Horizon 2020 research and innovation programme via the ERC Starting Grant MUSTANG (grant agreement number 714907). ES acknowledges fund-

ing from the European Research Council (ERC) under the European Union’s Horizon 2020 research and innovation program (grant agreement No. 694343). GB is supported by CONICYT/FONDECYT, Programa de Iniciación, Folio 11150220. FB acknowledges funding from the European Union’s Horizon 2020 research and innovation program (grant agreement No 726384 - EMPIRE). APSH is a fellow of the International Max Planck Research School for Astronomy and Cosmic Physics at the University of Heidelberg (IMPRS-HD). KK gratefully acknowledges support

Table 2. Measurements for each galaxy at 120 pc beam of CO maps.

Galaxies	Morphology	distance Mpc	inclination degree	$\log_{10} M_*$ M_{\odot}	$\log_{10} \text{SFR}$ $M_{\odot} \text{ yr}^{-1}$	# l.o.s	$\log_{10} \tau_{\text{ff}}$ years	$\log_{10} \tau_{\text{dep}}^{\text{mol}}$ years	$\log_{10} \epsilon_{\text{ff}}$	C	f_C	$\alpha_{\text{CO}}(1-0)$ (see notes)
NGC 0224	Sb-A	0.8	77.7	11.20	-0.43	22	$7.72^{+0.03(+0.18)}$ $-0.06(-0.30)$	$9.29^{+0.11(+0.07)}$ $-0.08(-0.14)$	$-1.56^{+0.09(+0.65)}$ $-0.15(-0.05)$	$0.97^{+0.10}$ -0.05	$1.01^{+0.01}$ -0.01	5.10
NGC 6744	Sbc-AB	11.6	40.0	10.90	0.39	299	$7.19^{+0.05(+0.04)}$ $-0.05(-0.02)$	$9.25^{+0.11(+0.02)}$ $-0.10(-0.06)$	$-2.07^{+0.13(+0.16)}$ $-0.10(-0.00)$	$0.67^{+0.15}$ -0.17	$1.05^{+0.02}$ -0.02	4.59
NGC 4321	Sbc-AB	15.2	27.0	10.90	0.53	525	$7.07^{+0.09(+0.04)}$ $-0.15(-0.00)$	$9.31^{+0.13(+0.07)}$ $-0.15(-0.06)$	$-2.25^{+0.20(+0.14)}$ $-0.22(-0.04)$	$0.65^{+0.19}$ -0.31	$1.05^{+0.05}$ -0.03	4.29
NGC 4303	Sbc-AB	17.6	25.0	10.90	0.72	424	$6.97^{+0.08(+0.08)}$ $-0.10(-0.03)$	$9.14^{+0.14(+0.07)}$ $-0.20(-0.06)$	$-2.14^{+0.18(+0.13)}$ $-0.23(-0.11)$	$0.75^{+0.13}$ -0.26	$1.03^{+0.04}$ -0.02	5.10
NGC 5194	Sbc-A	7.6	21.0	10.89	0.43	100	$6.79^{+0.12(+0.08)}$ $-0.09(-0.00)$	$9.36^{+0.14(+0.10)}$ $-0.13(-0.05)$	$-2.55^{+0.15(+0.14)}$ $-0.20(-0.10)$	$0.90^{+0.06}$ -0.17	$1.01^{+0.01}$ -0.01	4.35
NGC 4254	Sc-A	16.8	27.0	10.80	0.68	553	$7.03^{+0.12(+0.08)}$ $-0.16(-0.00)$	$9.22^{+0.12(+0.05)}$ $-0.17(-0.05)$	$-2.18^{+0.20(+0.13)}$ $-0.26(-0.05)$	$0.76^{+0.15}$ -0.26	$1.03^{+0.04}$ -0.02	4.41
NGC 4535	Sc-AB	15.8	40.0	10.60	0.30	314	$7.10^{+0.08(+0.07)}$ $-0.14(-0.00)$	$9.22^{+0.12(+0.06)}$ $-0.18(-0.06)$	$-2.19^{+0.19(+0.20)}$ $-0.24(-0.00)$	$0.63^{+0.15}$ -0.16	$1.05^{+0.03}$ -0.02	4.04
NGC 3627	Sb-AB	8.3	62.0	10.60	0.10	153	$7.02^{+0.11(+0.19)}$ $-0.22(-0.04)$	$9.25^{+0.14(+0.13)}$ $-0.18(-0.05)$	$-2.23^{+0.19(+0.40)}$ $-0.23(-0.00)$	$0.89^{+0.06}$ -0.10	$1.02^{+0.01}$ -0.01	4.18
NGC 3351	Sb-B	10.0	41.0	10.50	0.11	93	$7.29^{+0.05(+0.02)}$ $-0.15(-0.10)$	$9.16^{+0.11(+0.12)}$ $-0.27(-0.08)$	$-1.95^{+0.13(+0.24)}$ $-0.31(-0.06)$	$0.76^{+0.16}$ -0.12	$1.03^{+0.02}$ -0.02	3.98
NGC 1672	Sb-B	11.9	40.0	10.50	0.48	172	$7.04^{+0.05(+0.05)}$ $-0.34(-0.02)$	$9.03^{+0.13(+0.13)}$ $-0.14(-0.06)$	$-1.99^{+0.21(+0.22)}$ $-0.47(-0.09)$	$0.69^{+0.17}$ -0.19	$1.04^{+0.01}$ -0.02	4.21
NGC 0628	Sc-A	9.0	6.5	10.30	-0.02	208	$7.14^{+0.05(+0.07)}$ $-0.07(-0.05)$	$9.24^{+0.09(+0.09)}$ $-0.16(-0.06)$	$-2.08^{+0.13(+0.10)}$ $-0.13(-0.16)$	$0.80^{+0.06}$ -0.10	$1.03^{+0.01}$ -0.01	5.39
NGC 5068	Scd-AB	9.0	26.9	10.10	-0.59	30	$7.17^{+0.05(+0.07)}$ $-0.03(-0.11)$	$8.78^{+0.15(+0.21)}$ $-0.15(-0.08)$	$-1.58^{+0.12(+0.15)}$ $-0.15(-0.31)$	$0.60^{+0.05}$ -0.08	$1.06^{+0.01}$ -0.01	7.10
NGC 2835	Sc-B	10.1	56.4	9.90	-0.40	23	$7.34^{+0.02(+0.04)}$ $-0.05(-0.14)$	$8.87^{+0.16(+0.28)}$ $-0.18(-0.07)$	$-1.58^{+0.19(+0.27)}$ $-0.12(-0.25)$	$0.44^{+0.08}$ -0.11	$1.08^{+0.02}$ -0.01	8.30
NGC 0598	Scd-A	0.9	58.0	9.65	-0.35	19	$7.52^{+0.02(+0.06)}$ $-0.03(-0.29)$	$9.14^{+0.13(+0.31)}$ $-0.04(-0.00)$	$-1.64^{+0.07(+0.22)}$ $-0.09(-0.45)$	$0.85^{+0.04}$ -0.05	$1.02^{+0.01}$ -0.01	8.95

NOTE—Aliases for NGC 224, NGC 598, and NGC 5194 are M31, M33, and M51, respectively. The values of τ_{ff} , $\tau_{\text{dep}}^{\text{mol}}$, and ϵ_{ff} are for SFR(FUV+22 μ m), $H = 100$ pc, $C < 1$, and Galactic α_{CO} . We provide the scatter of measurements (+/- sign) as the range between 16th and 84th percentiles. The systematic uncertainties, defined as the largest difference between the median quantities from various assumptions, are written inside the parentheses. The standard errors of the median are very small ($\lesssim 0.01$ dex), and so not reported. Units of metallicity dependent $\alpha_{\text{CO}}(1-0)$ are $M_{\odot} [\text{K km s}^{-1} \text{ pc}^2]^{-1}$.

from grant KR 4598/1-2 from the DFG Priority Program 1573. The work of ECO is supported by the NSF under grant No. 1713949. ER acknowledges the support of the Natural Sciences and Engineering Research Council of Canada (NSERC), funding reference number RGPIN-2017-03987.

AU acknowledges support from Spanish MINECO grants ESP2015-68964 and AYA2016-79006. We acknowledge the usage of the Extragalactic Distance Database³ (Tully et al. 2009), the HyperLeda database⁴ (Makarov et al. 2014), the NASA/IPAC Extragalactic Database⁵, and the SAO/NASA Astrophysics Data System⁶.

REFERENCES

- Agertz, O., & Kravtsov, A. V. 2015, *ApJ*, **804**, 18
- Barnes, A. T., Longmore, S. N., Battersby, C., et al. 2017, *MNRAS*, **469**, 2263
- Bertoldi, F., & McKee, C. F. 1992, *ApJ*, **395**, 140
- Beuther, H., Meidt, S., Schinnerer, E., Paladino, R., & Leroy, A. 2017, *A&A*, **597**, A85
- Bigiel, F., Leroy, A. K., Jiménez-Donaire, M. J., et al. 2016, *ApJL*, **822**, L26
- Bolatto, A. D., Wolfire, M., & Leroy, A. K. 2013, *ARA&A*, **51**, 207
- Bolatto, A. D., Wong, T., Utomo, D., et al. 2017, *ApJ*, **846**, 159
- Caldú-Primo, A., & Schruba, A. 2016, *AJ*, **151**, 34
- Croxall, K. V., Pogge, R. W., Berg, D. A., Skillman, E. D., & Moustakas, J. 2015, *ApJ*, **808**, 42
- Druard, C., Braine, J., Schuster, K. F., et al. 2014, *A&A*, **567**, A118
- Evans, II, N. J., Heiderman, A., & Vutisalchavakul, N. 2014, *ApJ*, **782**, 114
- Federrath, C. 2015, *MNRAS*, **450**, 4035
- Federrath, C., & Klessen, R. S. 2012, *ApJ*, **761**, 156
- Gallagher, M. J., Leroy, A. K., Bigiel, F., et al. 2018, *ApJ* in press, arXiv:1803.10785, arXiv:1803.10785
- Gao, Y., & Solomon, P. M. 2004a, *ApJS*, **152**, 63
- , 2004b, *ApJ*, **606**, 271
- García-Burillo, S., Usero, A., Alonso-Herrero, A., et al. 2012, *A&A*, **539**, A8
- Gratier, P., Braine, J., Schuster, K., et al. 2017, *A&A*, **600**, A27
- Heyer, M., & Dame, T. M. 2015, *ARA&A*, **53**, 583
- Jarrett, T. H., Masci, F., Tsai, C. W., et al. 2013, *AJ*, **145**, 6
- Kennicutt, R. C., & Evans, N. J. 2012, *ARA&A*, **50**, 531
- Kim, C.-G., Ostriker, E. C., & Kim, W.-T. 2013, *ApJ*, **776**, 1
- Kruijssen, J. M. D., & Longmore, S. N. 2014, *MNRAS*, **439**, 3239
- Kruijssen, J. M. D., Longmore, S. N., Elmegreen, B. G., et al. 2014, *MNRAS*, **440**, 3370
- Kruijssen, J. M. D., Schruba, A., Hygate, A. P. S., et al. 2018, *MNRAS* in press, arXiv:1805.00012

³ <http://edd.ifa.hawaii.edu/index.html>

⁴ <http://leda.univ-lyon1.fr>

⁵ <http://ned.ipac.caltech.edu>

⁶ <http://www.adsabs.harvard.edu>

- Krumholz, M. R. 2014, *PhR*, 539, 49
- Krumholz, M. R., Dekel, A., & McKee, C. F. 2012, *ApJ*, 745, 69
- Krumholz, M. R., & McKee, C. F. 2005, *ApJ*, 630, 250
- Krumholz, M. R., & Tan, J. C. 2007, *ApJ*, 654, 304
- Lang, D. 2014, *AJ*, 147, 108
- Lee, E. J., Miville-Deschênes, M.-A., & Murray, N. W. 2016, *ApJ*, 833, 229
- Leroy, A. K., Bolatto, A., Gordon, K., et al. 2011, *ApJ*, 737, 12
- Leroy, A. K., Walter, F., Sandstrom, K., et al. 2013, *AJ*, 146, 19
- Leroy, A. K., Hughes, A., Schrubba, A., et al. 2016, *ApJ*, 831, 16
- Leroy, A. K., Schinnerer, E., Hughes, A., et al. 2017a, *ApJ*, 846, 71
- Leroy, A. K., Usero, A., Schrubba, A., et al. 2017b, *ApJ*, 835, 217
- Longmore, S. N., Bally, J., Testi, L., et al. 2013, *MNRAS*, 429, 987
- Makarov, D., Prugniel, P., Terekhova, N., Courtois, H., & Vauglin, I. 2014, *A&A*, 570, A13
- Martin, C., & GALEX Team. 2005, in *IAU Symposium*, Vol. 216, *Maps of the Cosmos*, ed. M. Colless, L. Staveley-Smith, & R. A. Stathakis, 221
- McKee, C. F., & Ostriker, E. C. 2007, *ARA&A*, 45, 565
- Meidt, S. E., Schinnerer, E., García-Burillo, S., et al. 2013, *ApJ*, 779, 45
- Meidt, S. E., Schinnerer, E., van de Ven, G., et al. 2014, *ApJ*, 788, 144
- Meidt, S. E., Leroy, A. K., Rosolowsky, E., et al. 2018, *ApJ*, 854, 100
- Miville-Deschênes, M.-A., Murray, N., & Lee, E. J. 2017, *ApJ*, 834, 57
- Mooney, T. J., & Solomon, P. M. 1988, *ApJL*, 334, L51
- Murray, N. 2011, *ApJ*, 729, 133
- Murray, N., Quataert, E., & Thompson, T. A. 2010, *ApJ*, 709, 191
- Ochsendorf, B. B., Meixner, M., Roman-Duval, J., Rahman, M., & Evans, II, N. J. 2017, *ApJ*, 841, 109
- Ostriker, E. C., McKee, C. F., & Leroy, A. K. 2010, *ApJ*, 721, 975
- Ostriker, E. C., & Shetty, R. 2011, *ApJ*, 731, 41
- Padoan, P., Haugbølle, T., & Nordlund, Å. 2012, *ApJL*, 759, L27
- Peek, J. E. G., & Schiminovich, D. 2013, *ApJ*, 771, 68
- Pety, J., Schinnerer, E., Leroy, A. K., et al. 2013, *ApJ*, 779, 43
- Pilyugin, L. S., Vílchez, J. M., & Contini, T. 2004, *A&A*, 425, 849
- Querejeta, M., Meidt, S. E., Schinnerer, E., et al. 2015, *ApJS*, 219, 5
- Raskutti, S., Ostriker, E. C., & Skinner, M. A. 2016, *ApJ*, 829, 130
- Rosolowsky, E., & Simon, J. D. 2008, *ApJ*, 675, 1213
- Saintonge, A., Kauffmann, G., Wang, J., et al. 2011, *MNRAS*, 415, 61
- Sakamoto, S., Hasegawa, T., Handa, T., Hayashi, M., & Oka, T. 1997, *ApJ*, 486, 276
- Sandstrom, K. M., Leroy, A. K., Walter, F., et al. 2013, *ApJ*, 777, 5
- Schinnerer, E., Meidt, S. E., Pety, J., et al. 2013, *ApJ*, 779, 42
- Schlegel, D. J., Finkbeiner, D. P., & Davis, M. 1998, *ApJ*, 500, 525
- Schruba, A., Leroy, A. K., Kruijssen, J. M. D., et al. 2017, *ApJ*, 835, 278
- Scott, D. W. 1992, *Multivariate Density Estimation*
- Sun, J., Leroy, A. K., Schrubba, A., et al. 2018, *ArXiv e-prints*, [arXiv:1805.00937](https://arxiv.org/abs/1805.00937)
- Tully, R. B., Rizzi, L., Shaya, E. J., et al. 2009, *AJ*, 138, 323
- Usero, A., Leroy, A. K., Walter, F., et al. 2015, *AJ*, 150, 115
- Utomo, D., Bolatto, A. D., Wong, T., et al. 2017, *ApJ*, 849, 26
- Vutisalchavakul, N., Evans, II, N. J., & Heyer, M. 2016, *ApJ*, 831, 73
- Yim, K., Wong, T., Howk, J. C., & van der Hulst, J. M. 2011, *AJ*, 141, 48
- Yim, K., Wong, T., Xue, R., et al. 2014, *AJ*, 148, 127